Article

Seismic Behavior of Demountable Self-Lock Joint for Middle Column Connection in Modular Steel Construction

Xiao-Meng Dai [1], Liang Zong [2,3,*], Yang Ding [2,3], Hao-Wen Zhang [2] and Feng-Wei Shi [2]

[1] China Railway Construction Bridge Engineering Bureau Group Corporation, Ltd., Tianjin 300300, China; raptor616888964@126.com
[2] School of Civil Engineering, Tianjin University, Tianjin 300072, China; dingyang@tju.edu.cn (Y.D.); haowenzhang158@outlook.com (H.-W.Z.); shifengwei@tju.edu.cn (F.-W.S.)
[3] Key Laboratory of Coast Civil Structure Safety, Ministry of Education, Tianjin University, Tianjin 300072, China
[*] Correspondence: zongliang@tju.edu.cn

Abstract: The use of modular steel construction (MSC) achieves a minimum of on-site work and the potential for removability and reuse. In order to realize the overall disassembly of module buildings and the rapid off-site reconstruction after disassembly, special requirements are put forward for the joints of MSCs. The existing joints of MSCs have some problems, such as the difficulty in the erection of the joints for middle column connection and their inability to be reused. In order to solve these key technical problems, an improved version of the demountable self-locking joint is proposed based on the previous plug-in self-locking joint. For this new type of joint, a full-scale test consisting of four specimens was carried out. The results of functional tests verify that the joint has good demountability. The seismic behavior of the joint under seismic load was investigated by cyclic loading tests. Then, finite element (FE) models were developed and validated through the test results. The results of finite element parameter analysis show that joint boxes are very important to the initial stiffness of this kind of joint, but the thickness of the joint box and the diameter of the stud have little influence on the seismic behavior of the joint.

Keywords: full-scale tests; seismic behavior; modular steel construction; finite analysis; column-beam joint

1. Introduction

Modular steel construction (MSC) has been used widely due to its exceptional advantages: minimum of on-site work, and higher construction speed and qualities. Different from other types of construction, modular steel construction is highly integrated prefabricated. Due to these features, MSCs are an ideal construction for emergency situations (e.g., emergency hospital centers). Structural components and building services, i.e., electrics, pipelines, and decorations, are integrated into room modules, which are the basic units of modular steel construction. Each room module combines structural and architectural functioning, e.g., a living room module, a bathroom module, or a staircase. These room modules are off-site prefabricated and can be replaced easily. This feature of MSC provides the potential for removability and reuse. Thus, MSC can be adapted to temporary and movable buildings.

The connecting joints of modular steel construction are very different from that of regular steel structures [1]. Figure 1 compares the joints in a regular structure and MSC. In joints of a regular structure, there are four beams and one continuous column. In joints of MSC, the numbers are sixteen and eight. Additional special requirements should be fulfilled for the MSC joints: good cooperation with other installed structure components and building services, minimum need of construction spaces and time, and potential to be demounted. Joints with mechanical connections are recommended due to good

detachability. One of the key issues of MSC joints is the operation spaces for installation or uninstallation. As shown in Figure 2, there are three types of joints for modular steel construction, i.e., side, corner, and middle joints. Among these joints, the side and corner joints will not be limited by operation spaces. But for the middle joints, there is no access from outside. As the walls, doors, floors, and ceilings were installed before the assembling, there are no operation spaces for the connection of joints.
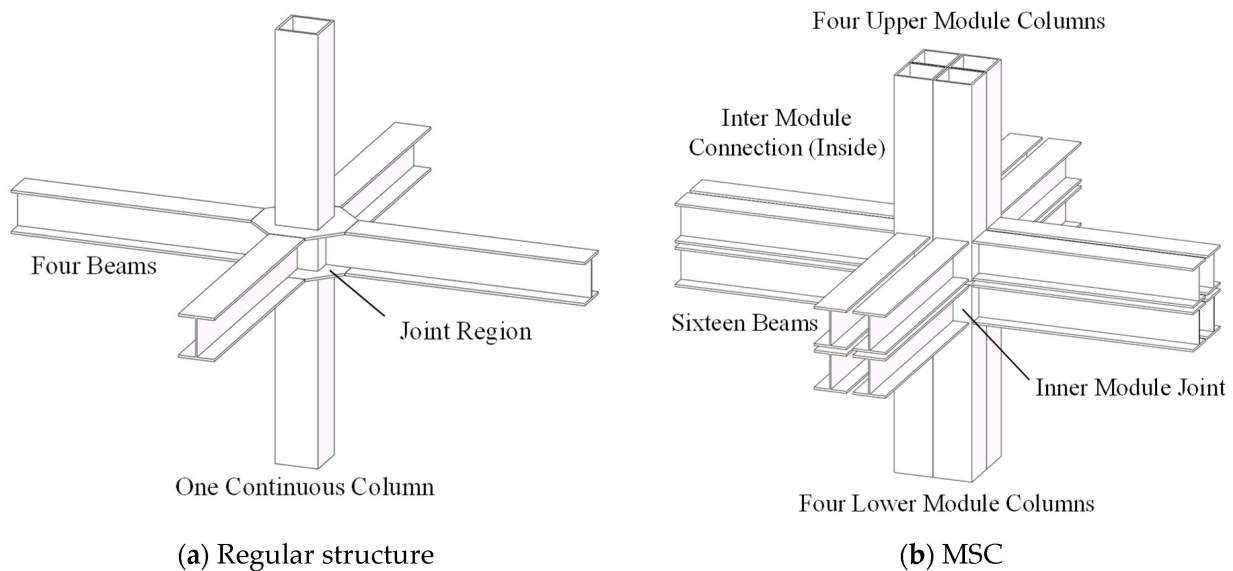

(**a**) Regular structure   (**b**) MSC

Figure 1. Comparison of joints in regular structure and MSC.

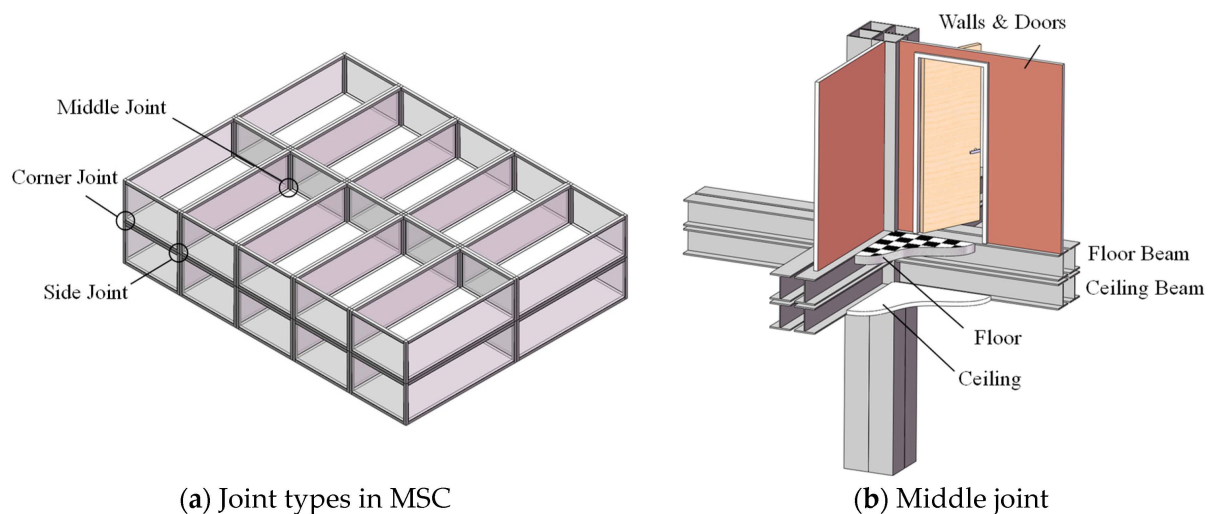(**a**) Joint types in MSC   (**b**) Middle joint

Figure 2. Joint in modular steel construction.

Previous research has provided various types of mechanical-connecting joints for modular steel construction. Lawson proposed bolt-connecting joints for a square hollow section or open section column, as shown in Figure 3a [2]. These types of joints can be used as side or corner joints for modular steel construction, but cannot be used as middle joints. The end plates of the upper and lower module columns are connected with bolts. For square hollow section columns, access holes are set for installation or uninstallation. Chen developed bolt-connecting joints with a plug-in for square hollow section columns [3,4]. These types of joints can be used as middle or side joints for modular steel construction. Upper and lower modules are connected by long penetrating bolts at the end of the beams. A plug-in component is set between the upper and lower square hollow section columns.

The vertical load cannot be transferred between the upper and lower columns directly. Moreover, the penetrating long bolts will interfere in the installation of other structure components, e.g., wall plates. Ding developed blind bolt-connecting joints with a plug-in for square hollow section columns, as shown in Figure 3b. These types of joints can be used as side joints for modular steel construction, but cannot be used as middle joints. Similar to the joints of Chen, a plug-in component is set between the upper and lower square hollow columns. The columns are connected to the plug-in component with blind bolts, which only require one-side operation. Though many other joints were proposed, analyzed, and tested, the problems of joints for modular steel construction still exist [5–9]. Joints for modular steel construction still need to be improved.
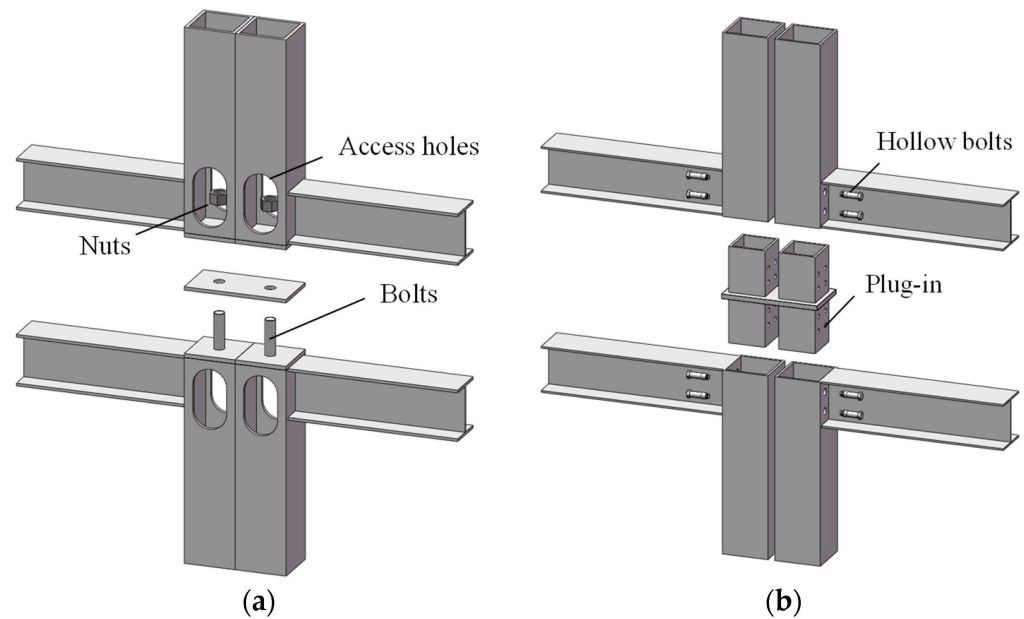

Figure 3. Previous joints for MSC: (**a**) Lawson [2]. (**b**) Ding [10].

The most common modular buildings also include the steel frame modular, which consists of the full length of beams and girders, and column ends and requires beam-column bolt connections at each floor. Chen developed a new type of f site-bolted assembled joint for prefabricated modular H-shaped steel-beam-column joints [11]. The assembly diagram of joints is shown in Figure 4a. The developed joint assembles the columns and beams at the connector region through on-site bolting of the column base plate and beams' splice plate, avoiding direct welding of the structural components to each other. Du proposed a beam-through moment-resisting joint for H-section (wide-flange) beams and columns that can be prefabricated [12]. The joints erect an entire floor by bolting the upper-level columns to the lower-level beams, as shown in Figure 4b. With this type of beam-through beam-column joint, it is feasible to offset columns on adjacent floors and increase the flexibility and versatility of the framing plan layout.

Self-lock joints for modular steel construction were proposed to solve this middle joint connection issue [13]. These self-lock joints need no operation spaces during both the connection and disconnection processes, and can be demounted easily due to the unlocking device. Meanwhile, the joints have no interruptions with other integrated structural components and services, and no limitations to sections of beams or columns. Thus, this type of joint can be used as a middle joint for modular steel construction.

Although more and more new modular joints have been developed in recent years, there are still considerable difficulties in realizing the overall disassembly of module buildings and the rapid off-site reconstruction after disassembly. In this follow-up research, the self-lock plug-in connector was improved. A set of unlocking devices was added for easier disconnection of the joint. This improvement could increase the

speed of the demountable function for the joints, which helps to further realize the overall disassembly of module buildings. A full-scale test consisting of four specimens is reported in the following part of this paper. The demounting processes of the joints were verified through a functional test. Then, the full-scale specimens were applied with cyclic load to investigate the seismic behavior. Finite element (FE) models of these novel joints were developed and validated with the test results. Parameter analysis was conducted based on the FE models.
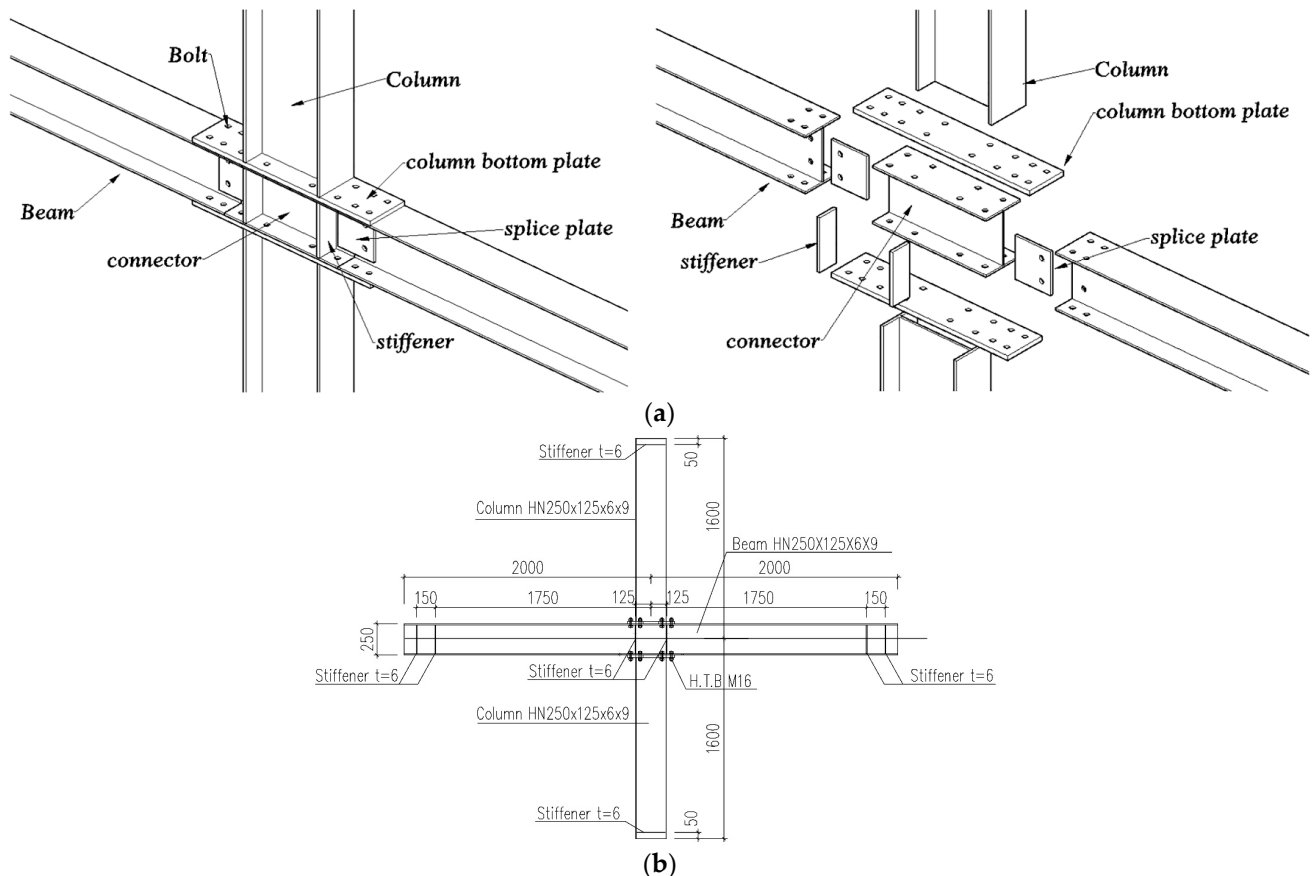

Figure 4. Joints for steel frame modular: (**a**) Chen [11]. (**b**) Du [12].

2. Mechanism of Self-Lock Joint

2.1. Self-Lock Connector and Unlocking Device

The key components of the novel joint are a self-lock connector and an unlocking device. This connector is developed based on the previous self-lock plug-in connector and a set of unlocking devices is added [14]. The unlocking device is an additional device that provides an easy way to demount and reuse the room module in modular steel construction. The mechanism of the connector is shown in Figure 5. Components of this connector can be divided into two sets: unlocking components (Component 1–3) and self-lock connecting components (Component 4–15). The key components of this connector are an unlocking hydraulic jack (1), safe spring (4), acting spring (6), trigger block (7), sleeve (12), cone-shaped latches (13), and stud (15). The unlocking hydraulic jack is integrated into this connector and can be powered by an external hydraulic pump, which is not shown in the figure. The safe and action springs are pre-compressed to certain compressive forces, respectively. The cone-shaped latches consist of four cone-shaped quarter orientation components. The inner surface of the cone-shaped latches is fabricated with ring-teeth and the outer surface is a cone surface. A trigger block is set between the four cone-shaped latches before connecting. As the diameter of the trigger block is higher than the diameter of the inner hole of the latches, the closing trend of the cone-shaped latches is blocked.

The sleeve is a circle-shaped component, with a step on the outer surface to hold the acting spring. The inner surface of the sleeve is the cone surface, which can fit with the cone-shaped latches. The stud is a rod with ring-teeth and is fixed on the top surface of the lower module column. The pull side of the ring-teeth on the stud fit tightly with that on the cone-shaped latches. A clearance is set to allow machining errors and dust. The working process can be divided into these four phases below.
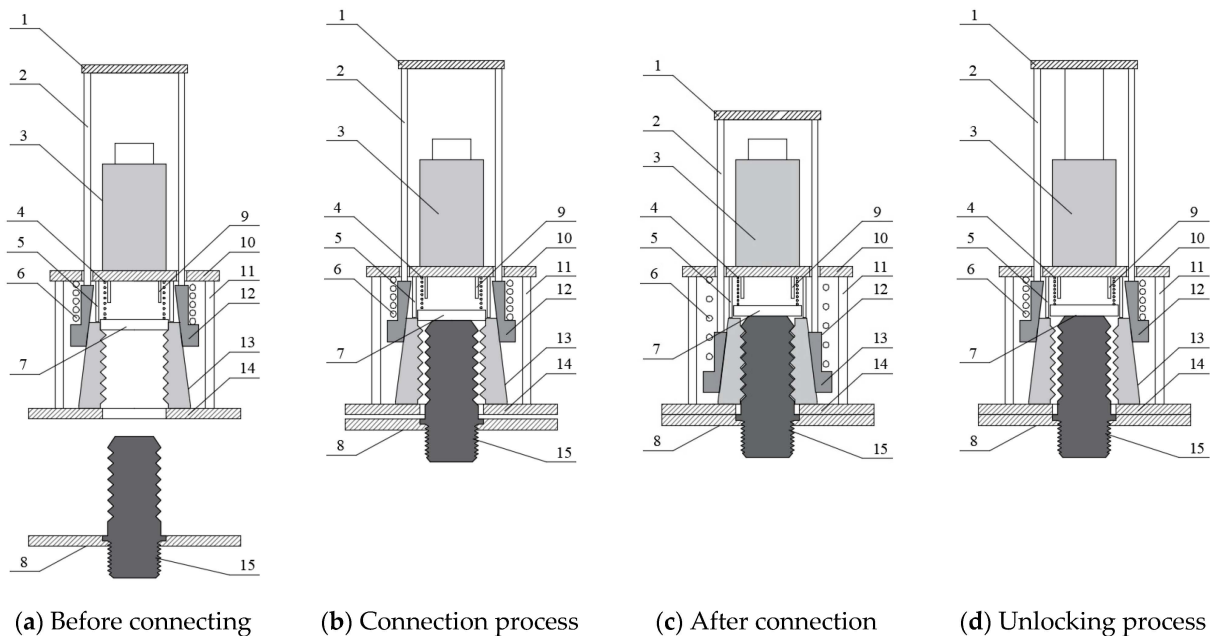

(**a**) Before connecting (**b**) Connection process (**c**) After connection (**d**) Unlocking process

Figure 5. Mechanism of self-lock connector and unlocking device: 1—unlock plate, 2—unlock bar, 3—unlock hydraulic jack, 4—safe spring, 5—outer barrel, 6—action spring, 7—trigger block, 8—top surface of the lower module column, 9—inner barrel, 10—locating plate, 11—locating screw, 12—sleeve, 13—cone—shaped latches, 14—bottom surface of upper module column, 15—stud.

Figure 5a shows the phase before connecting. The sleeve and cone-shaped latches are compressed by the action spring. The closing trend of the cone-shaped latches is still blocked by the trigger plate. The spacing between the latches is larger than the diameter of the stud and allows the stud to plug in.

During the connection process, the upper module is placed onto the lower module so that the stud is plugged into the spacing of the cone-shaped latches, as shown in Figure 5b. The stud pushes the trigger plate out of the cone-shaped latches. Without the trigger block, the sleeve moves under the compressive force of the action spring and forces the latches to close. The ring-teeth on the stud and the cone-shaped latches fit tightly. Machining errors can be eliminated automatically due to the wedging effect.

Figure 5c shows the working phase after connection. After the connection is made, this connector can resist the pull force. The pull force can be transferred through the ring-teeth on the stud and the cone-shaped latches. Because the angle of the cone surfaces between the sleeve and the cone-shaped latches is smaller than the friction angle of the steel material, the connector is friction-locked and will not come loose. Thus, the separation between the upper and lower modules is prevented and the pull force is transferred.

Figure 5d shows the unlocking process of the connector. When it is necessary to disconnect the upper and lower modules, the unlocking device is needed. The unlocking hydraulic jack is powered by an external pump and the piston of the jack extends. The piston pushes the unlocking plate and drives the sleeve to move upward. Without the constraint of the sleeve, the cone-shaped latches can be open. The stud can be pulled out and the connector is unlocked. After the unlocking process, the connector can be reset and will be functional.

2.2. Demountable Self-Lock Joint in Modular Steel Construction

The demountable self-lock joint can be used as corner, side, and middle joints in modular steel construction, as shown in Figure 6. Joint boxes are set at the corners of each module and are welded to beams and columns. The stud is fixed on the top surface of the lower module column while the other components of the self-lock connector are set inside the joint box. A soft hydraulic tube is integrated into the joint. One end of the tube is connected to the unlocking hydraulic jack, the other end is set outside of the joint in case of the unlocking process. For side and middle joints, a connecting plate is needed to connect the two (for side joint) or four (for middle joint) modules in the same story, as shown in Figure 6b,c. Matching holes are fabricated on the connecting plate to allow the studs through. The connecting plate is bolted on the top surfaces of lower module joint boxes. The sunk bolts are used to flatten the top surface of the connecting plate.
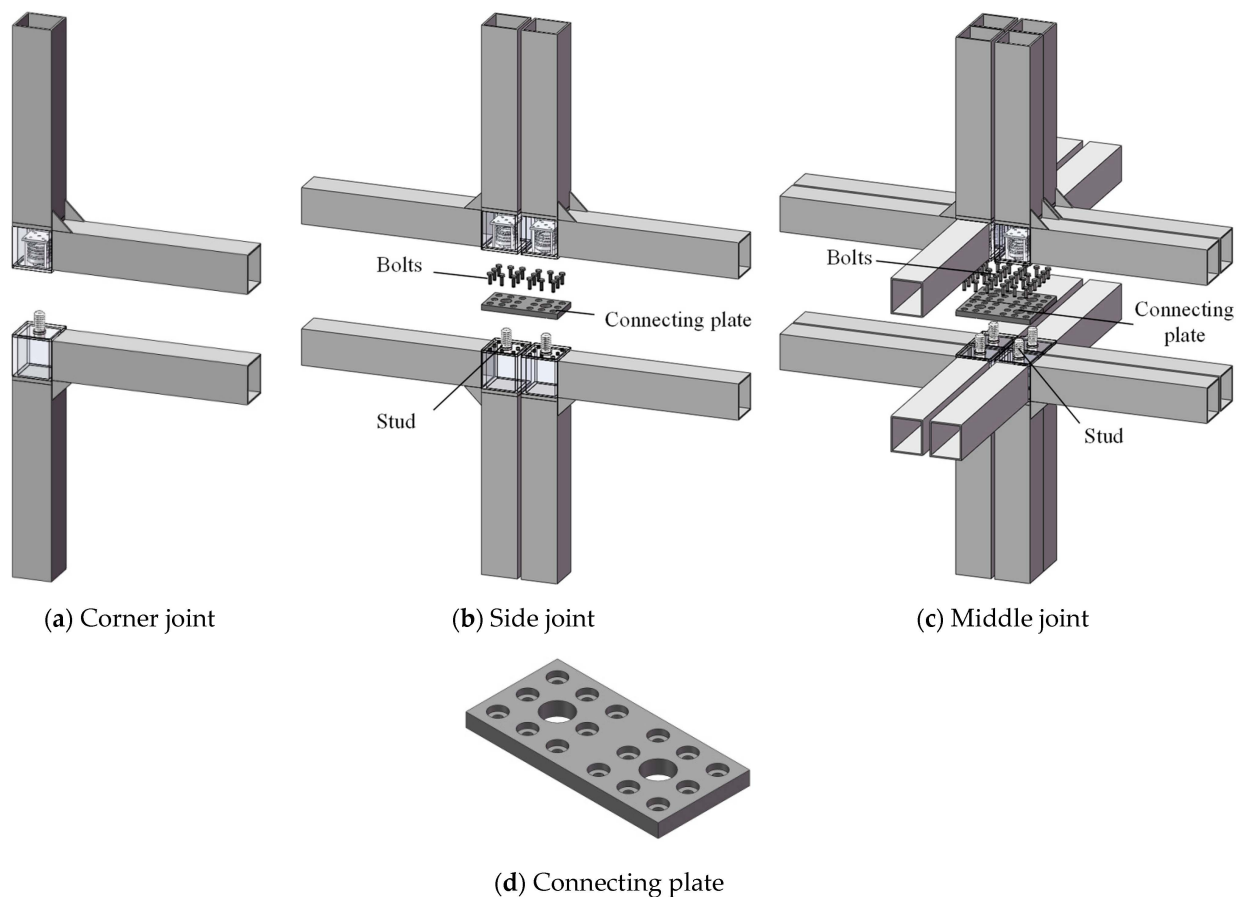

(**a**) Corner joint   (**b**) Side joint   (**c**) Middle joint

(**d**) Connecting plate

Figure 6. Self-lock joints for modular steel construction.

With this novel joint, the modular steel construction can be assembled or disassembled by a crane. Room modules can be piled up or removed as containers. Compared with previous joints, the characteristics of the novel joint include:

(a) No extra operation spaces are needed during the construction. The connecting process is performed automatically during the piling up of the modules. The on-site work is minimized. Thus, this novel joint provides an easy solution for middle joints of modular steel construction.

(b) The unlocking device of this joint provides exceptional detachability and interchangeability. Room modules can be easily detached and reused on another site. Thus, resources can be saved and the disruption to the environment can be minimized.

(c)   No limitations to sections of beams or columns are needed. This joint can be adapted to beams and columns with various types of sections. The choices of the beam and column sections are flexible.

3. Experimental Program

3.1. Specimen Design

The seismic behavior of T-shaped specimens has been tested in previous research [13]. This paper focused on the effect of unlocking devices and combined effect of cross-shaped joint specimens. A test on four full-scale specimens was conducted. Figure 7 and Table 1 shows the details of the specimens. These specimens can be divided into two groups. The specimens TS-1 and TS-2 were T-shaped specimens to investigate the effect of the unlocking devices. Specimen TS-1 was defined as a contrast specimen while specimen TS-2 was defined as a demountable specimen. For specimen TS-2, a set of unlocking devices was integrated and a 110×120 mm maintenance opening was set on the joint boxes, as shown in Figure 7c. The hydraulic tube that was connected to the unlocking jack extended to the outside and could be connected to a hydraulic pump. TS-3 and TS-4 were cross-shaped joint specimens to investigate the combined effect in middle joints. The difference between the two cross-shaped specimens was the thickness of the connecting plates, i.e., 20 mm (TS-3) and 30 mm (TS-4). The column and beam sections of the specimens were square hollow sections: $200 \times 200 \times 10$ (column), $200 \times 180 \times 8$ (floor beam), and $200 \times 180 \times 6$ (ceiling beam). The thickness of the joint boxes was set as 20 mm to ensure their strength and stiffness. Rib stiffeners were added at the corners.

Table 1. Specimens of Demountable Self-Lock Joint.

Specimen No.	Joint Type	Shape	Thickness of Connecting Plate (mm)	Remarks
TS-1 (Contrast)	Corner joint	T-shape	-	-
TS-2	Corner joint	T-shape	-	Unlocking device
TS-3	Side Joint	Cross-shape	20	-
TS-4	Side Joint	Cross-shape	30	-

(**a**) T-shaped specimens   (**b**) Cross-shaped specimens

Figure 7. *Cont.*

(**c**) Maintenance opening on TS-2
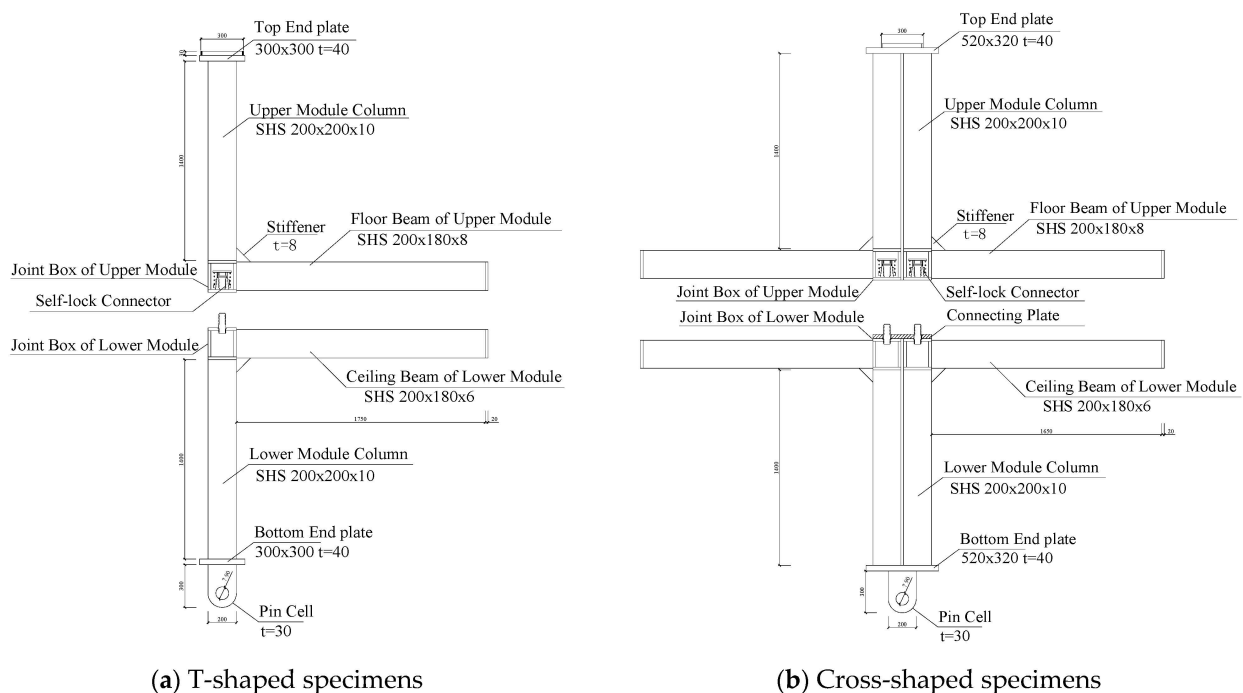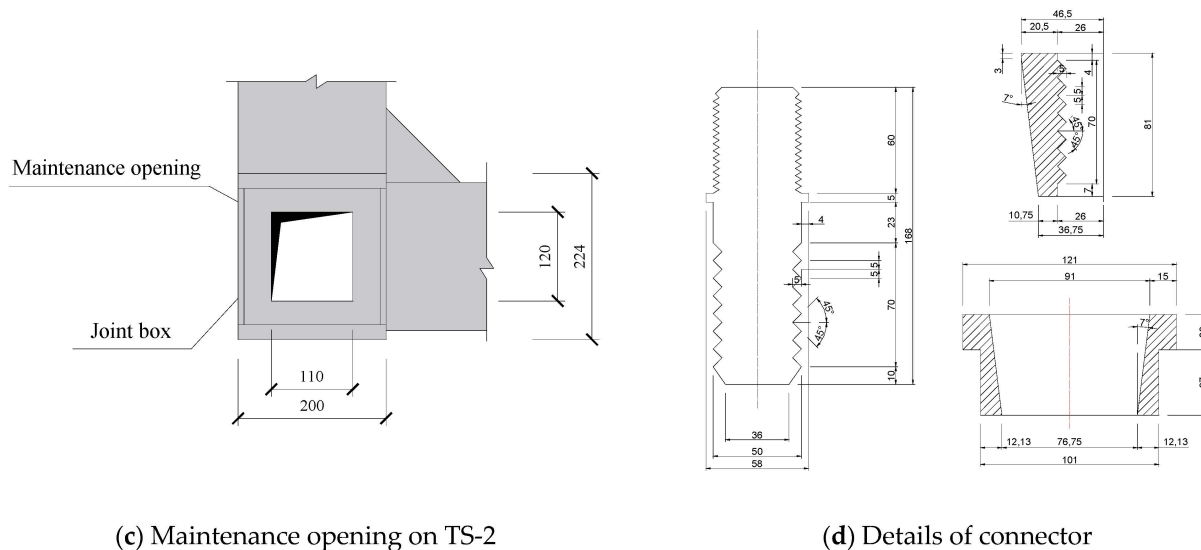
(**d**) Details of connector

Figure 7. Design of self-lock joints (mm).

The mechanical properties of the specimen were tested before the experimental study. Most components of the self-lock connector, including stud, sleeve, and cone-shaped latches, were fabricated with U20452 (45#) class steel. Columns, beams, and joint boxes were welded with a Q345B class steel plate. Coupon tests were performed according to Chinese standard GB/T 228.1-2010 [14]. Engineering tensile stress–strain curves are given in Figure 7. The results are listed in Table 2, showing the mechanical properties of the steel were qualified according to the Chinese standard GB/T 699-2015 and GB/T 1591-2018 [15,16].

Table 2. Mechanical Properties.

Parts	Steel Grade	Elastic Modulus (N/mm^2)	Yield Strength (N/mm^2)	Ultimate Strength (N/mm^2)	Ultimate Strain	Elongation (%)
Connector components	U20452 (45#)	193.3	441.3	553.7	0.170	30.6
Steel plate	Q345B	195.8	393.8	523.5	0.192	33.8

3.2. Experimental Program

The function of demounting was validated before loading the program. Figure 8 shows the demounting process of the specimen TS-2, which was equipped with an unlocking device. As shown in Figure 8a, the initial status of the specimen TS-2 was a whole. The extended hydraulic pipe, which was connected to the unlocking hydraulic jack in the joint box, was powered by an external pump. The unlocking device was activated and the connection was loosed. The upper module component could be lifted up by a crane, as shown in Figure 8b. The self-lock connector and the unlocking device were reset through the maintenance opening on the joint box and re-functioned after the reset. The specimen was re-connected, as shown in Figure 8c.

The setup of the loading program is shown in Figure 9. The testing devices and facilities included reaction wall, constraint frame, bottom base, reaction frames, and hydraulic jacks. The constraint frame was fixed on the side surface of the reaction walls with four 80 mm diameter bolts. The specimens were constrained at the end of the constraint frame. The bottom base was fixed on the ground and was pin-connected to the specimens. Only displacements were constrained while the rotations were not at the top or bottom of the specimens. A hydraulic jack was placed on the top surfaces of the specimens to provide vertical load during the loading program. The axial force hydraulic jack was supported by a reaction frame, which was not shown in Figure 9a. An axial

force of 150 kN (for T-shaped specimens) or 300 kN (for cross-shaped specimens) was applied and kept during the loading program. The nominal axial compression ratio of the columns was kept as 0.05. Two loading hydraulic jacks (one for T-shaped specimens) were fixed on the ground to apply load on the ends of the specimen beams. For cross-shaped specimens (TS-3 and TS-4), the load on the beams was rotational symmetric. As the floor and ceiling beams worked separately in practical construction, a special loading cell was designed to simulate the working conditions of the beams [17]. This loading cell released the horizontal displacements and constrained the vertical displacements at the ends of the beams. Thus, the combined effect of the two beam sections was avoided and the beams could work separately.
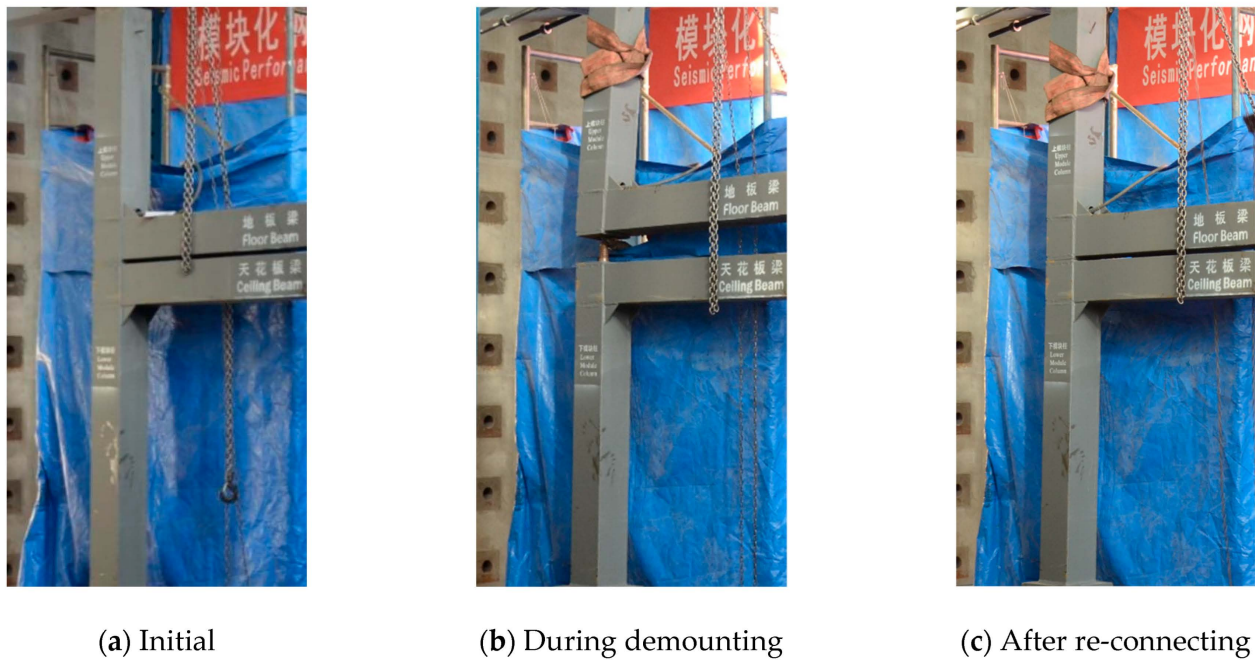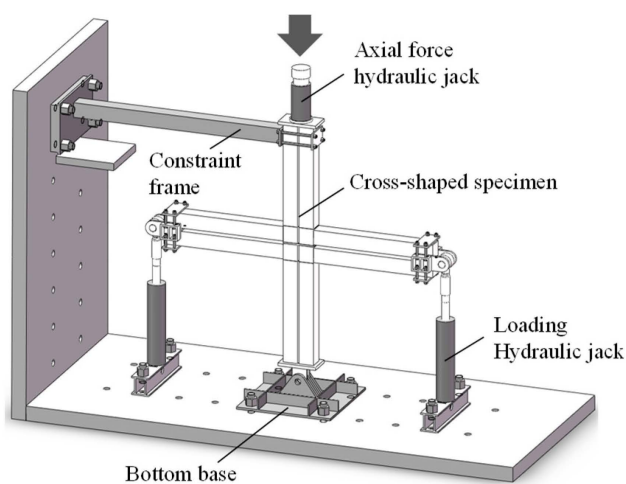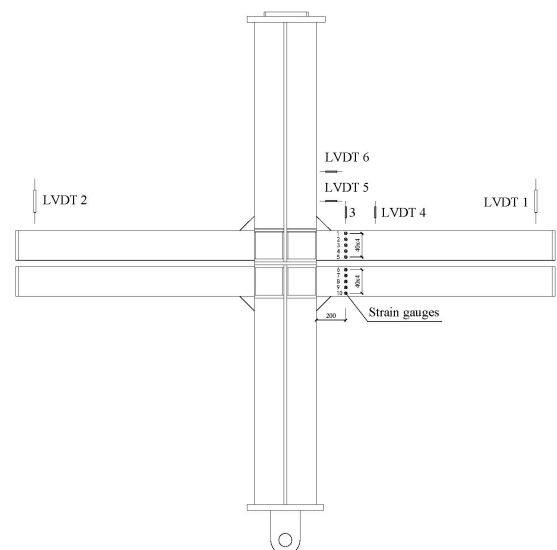

(**a**) Initial   (**b**) During demounting   (**c**) After re-connecting

Figure 8. Unlocking process of specimen (TS-2).

(**a**) Loading device   (**b**) Measurement

Figure 9. Test setup.

Displacement-controlled cyclic load was applied to the ends of the specimen beams according to standard ATC-24 [18], as shown in Figure 10. The yield displacement Δ_y was predicted as 30 mm before the test. Two cycles were loaded in each loading step except the yield phase. During the yield phase, three cycles were loaded at loading steps of 30, 45, and 60 mm.
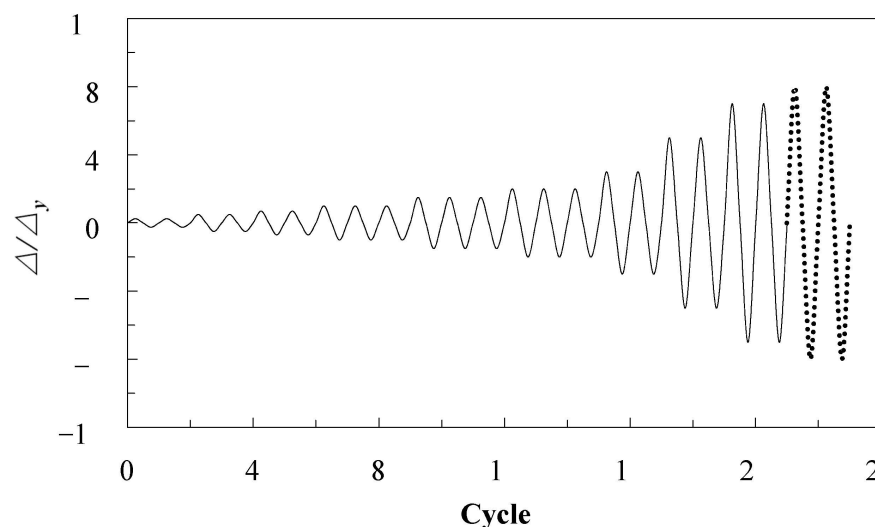

Figure 10. Cyclic loading protocol.

The measurement of the specimens is shown in Figure 9b. The axial and cyclic loads were measured by dynamic force sensors that were integrated into the hydraulic jacks. Seven linear variable differential transformers (LVDTs) were set to measure the vertical and horizontal displacements of the specimens. LVDT 1 and 2 were placed to measure the vertical displacement of the beam ends. They were also the control displacements during the loading program. Two pairs of LVDTs were set near the root of the beams and columns. LVDT 3 and 4 measured the vertical displacements of the right floor beam. LVDT 5 and 6 measured the horizontal displacements of the upper module column. With these two pairs of displacements, rotations of the beam and column sections at the root could be calculated. Strains on the specimens were measured by strain gauges.

4. Result and Discussion

4.1. General Behavior

4.1.1. T-Shaped Demountable Specimens (TS-1 and TS-2)

Seismic behavior of the contrast specimen TS-1 was reported in reference [13]. Moment–drift ratio curves of T-shaped specimens (TS-1 and TS-2) is shown in Figure 11. Compared with specimen TS-1, the demountable specimen TS-2 had a lower stiffness due to its opening on the joint box. The elastic stiffness of specimen TS-2 was lower than that of specimen TS-1 by 15%. During the first cycle of the loading step (drift ratio = 1.67%), paint wrinkled at the root of the ceiling beams. The moment–drift ratio curve bent slightly. A residual deformation of 1.1 mm was observed after the third cycle of this loading step. When the drift ratio reached 2.50%, i.e., point A in the moment–drift ratio curves, a continual sizzle sound was heard. Micro-cracks were observed at the corners of the ceiling beam section. The position of the cracks was just outside the stiffeners. Paint peeled off from the beam webs and flanges. After the drift ratio reached 3.33%, i.e., point B in the curves, local buckling occurred at the root of the ceiling beam. The flanges buckled inward while the webs buckled outward. The cracks extended on the ceiling beam, causing fractures at the corners of the beam. Figure 12a shows the extended cracks on the specimen beam. When the drift ratio reached 5.00%, the moment reached the maximum at point C and began to decrease. The maximum strengths of these specimens were close. The difference was not more than 10%. As the damage on the beam accumulated, the plastic hinge was observed

at the root of the ceiling beam. Slight local buckling was observed on the floor beam. After the drift ratio reached 6.67%, the ceiling beam was close to failure and lost most of its bearing capacity. Most of the load was taken by the floor beam. The local buckling on the floor beam was significant, as shown in Figure 12b. No cracks were observed on the floor beam. Rotation between the upper and lower modules occurred. A gap occurred on the original tight compressed surfaces of the joint boxes. As shown in Figure 12c, one side of the surface was compressed while the other side was open. These two sides switched with each other under the cyclic load. The upper and lower module columns were not in a straight line anymore, as shown in Figure 12d. The maximum angle between the upper and lower module columns was about 3.5°. When the drift ratio approached 8.33%, the cracks expanded with a loud noise. The load decreased to 85% of its maximum and the loading process was terminated.

(**a**) TS-1 (**b**) TS-2
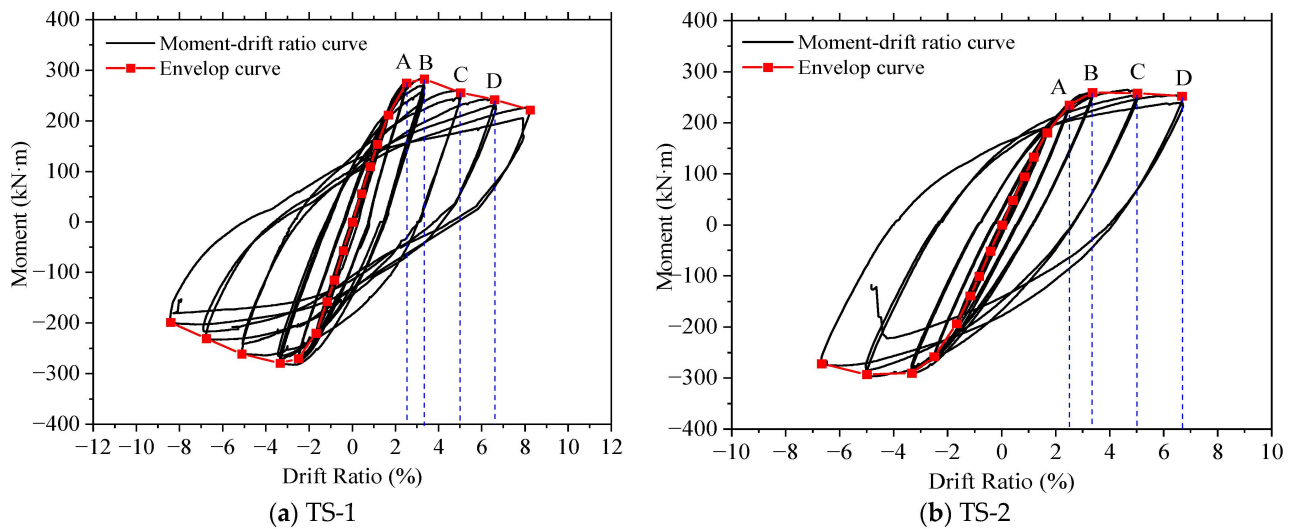
Figure 11. Moment–drift ratio curves of T-shaped specimens (TS-1 and TS-2).

(**a**) Cracks and local buckling on ceiling beam (**b**) Local buckling on floor beam

(**c**) Rotation and gap between joint boxes (**d**) Rotation between the columns

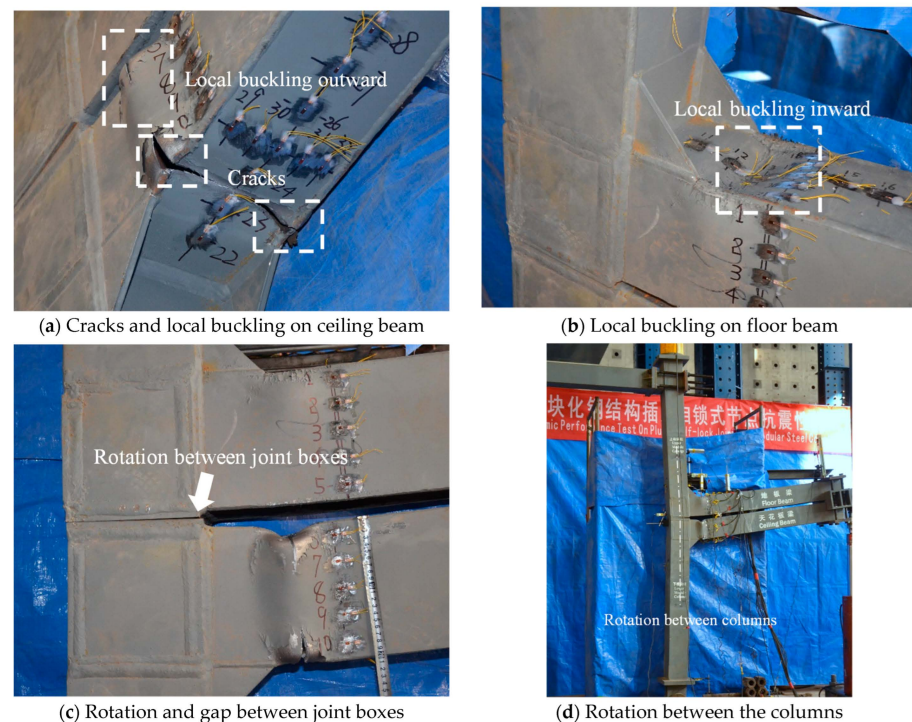**Figure 12.** Observations of the T-shaped specimens (TS-1 and TS-2).

The failure mode of these T-shaped specimens was the failure of the ceiling beams. The cracks at the corners of the ceiling beam section extended while the flanges and webs buckled. The position of the failure was at the root of the beam, just outside of the stiffeners. The floor beam was less damaged due to its thickness (8 mm vs. 6 mm). The columns and the joint boxes were elastic during the whole loading program.

4.1.2. Cross-Shaped Specimens (TS-3 and TS-4)

In general, the observations of the cross-shaped specimens were rotational symmetric. Local buckling, cracks, and plastic hinges were observed on both floor and ceiling beams, as shown in Figure 13a,b. The cracks penetrated the whole flange of the section. During the loading program, no relative rotation occurred between the upper and lower joint boxes, as shown in Figure 13c. The original compressed surfaces remain tight and no gap occurred. Figure 13d shows that the upper and lower columns were in a straight line. No defamations were observed on the connecting plate. Moment-drift ratio curves of the cross-shaped specimens (TS-1 and TS-2) are shown in Figure 14. According to the comparison between Figures 14a and 14b, the differences between specimens TS-3 and TS-4 were insignificant during the loading program, indicating that the seismic behavior of the specimens was not controlled by the thickness of the connecting plate. The failure mode of the cross-shaped specimens was the fracture of floor and ceiling beams. The fracture position was just outside of the stiffeners, the same as that in T-shaped specimens.
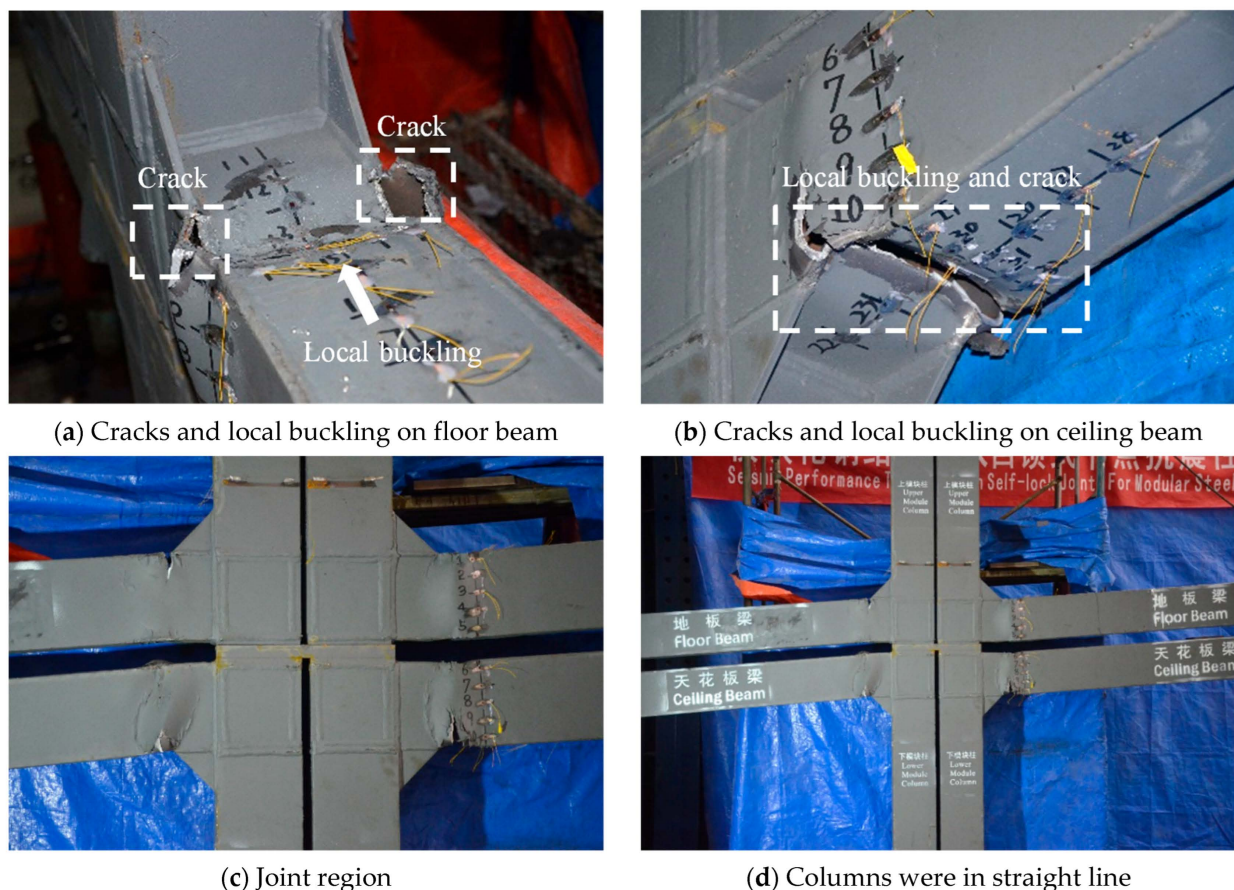

(**a**) Cracks and local buckling on floor beam

(**b**) Cracks and local buckling on ceiling beam

(**c**) Joint region

(**d**) Columns were in straight line

Figure 13. Observations of the Cross-shaped specimens (TS-3 and TS-4).
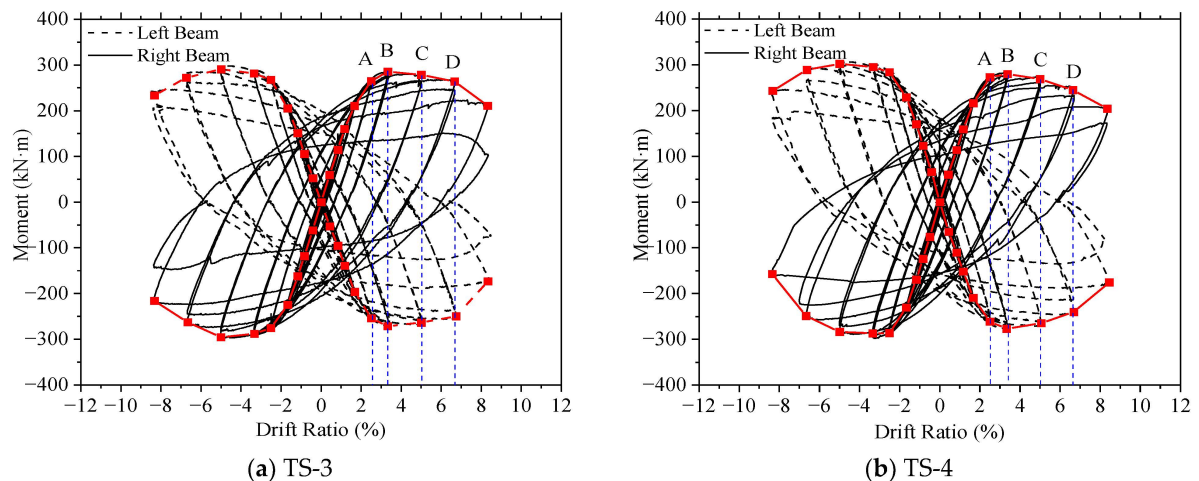
(**a**) TS-3

(**b**) TS-4

Figure 14. Moment-drift ratio curves of the cross-shaped specimens (TS-1 and TS-2).

4.2. Strength, Stiffness and Ductility

The moment–rotation envelop curves of the specimens are shown in Figure 15. The rotation was gained through the rotations of floor beam root and column root on the right side, which was measured by LVDT 3–6. Thus, the effect of the beam and column deformation can be eliminated. The stiffness of the specimens is between 0.5 EI/L and 8 EI/L. Moreover, the strength of the joints is higher than that of the floor and ceiling beams. Thus, these types of joints can be defined as semi-rigid full-strength joints [19].
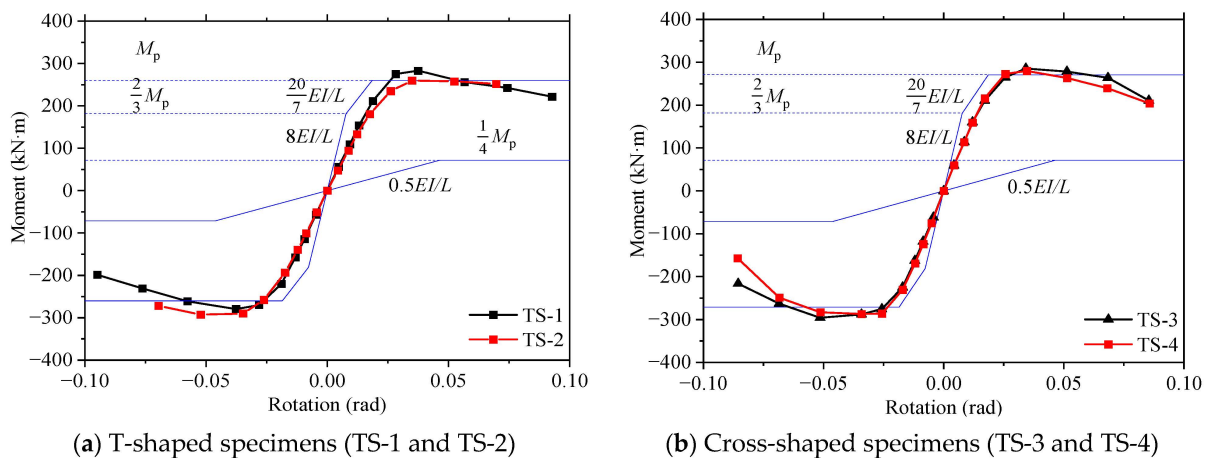

(**a**) T-shaped specimens (TS-1 and TS-2)

(**b**) Cross-shaped specimens (TS-3 and TS-4)

Figure 15. Moment-rotation envelop curves.

Two pairs of comparisons (TS-1 vs. TS-2, TS-3 vs. TS-4) are made, as shown in Figure 15a,b. The results show that the strength difference of the specimens was insignificant (lower than 8%). This indicates that the factor of unlocking the device and connecting plate will not affect the strength of the joints. The reason is that the failure mode of the joints is the fracture of the beams. As the strength of the joint region is much higher than that of the beam sections, the failure always occurs on the sections of the beam root. Thus, the failure mode is determined by the bending strength of beam sections.

The stiffness is calculated through the slope of the moment–drift ratio envelop curves, as shown in Figure 16. The stiffness curves are convex in shape. Also, comparisons of the specimens are made to investigate the effect of the factors. As shown in Figure 16a, the stiffness of specimen TS-1 is higher than that of the specimen TS-2 by about 15%. This is due to the opening on the joint box of the specimen TS-2. As the opening is essential for the reset of the unlocking device, it can be concluded that the factor of the unlocking device will weaken the stiffness of the joint. Figure 16b shows

the comparisons of four curves, i.e., both sides of specimen TS-3 and TS-4. These curves are in good coincidence and are symmetric in shape. That indicates that the thickness of the connecting plate does not affect the stiffness of the joint. It can also be concluded that the behavior of the joints is symmetric.
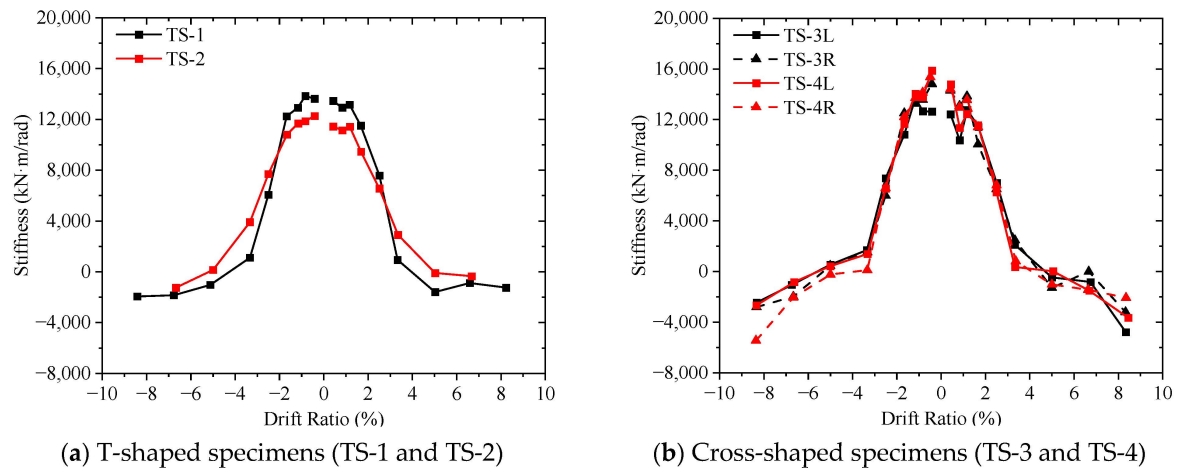

(a) T-shaped specimens (TS-1 and TS-2)   **(b)** Cross-shaped specimens (TS-3 and TS-4)

Figure 16. Stiffness degradation curves.

The angular displacement ductility coefficient (μ) is defined as the ratio between the failure inter-story drift ratio and the yielding inter-story drift ratio, as given in Equation (1).

$$\mu = \frac{\theta_y}{\theta_u} \tag{1}$$

Table 3 shows the ductility of the specimens. The ductility coefficients of the specimens are about 2.5–3.1. The results show that all the joints have good ductility. The ductility of the specimen TS-2 is lower than that of TS-1. This is due to the higher yield drift ratio of specimen TS-2. The lower stiffness of specimen TS-2 results in higher yield displacement. Meanwhile, the ultimate drift ratio is mainly determined by the beam section for these specimens. Thus, the ductility coefficient of specimen TS-2 is higher than that of the contrast specimen. For cross-shaped specimens, the effect of the connecting plate is insignificant.

Table 3. Strength and Ductility Coefficient.

| | | Yield Strength (kN·m) | | Maximum Strength (kN·m) | | Yield Drift Ratio (%) | Ultimate Drift Ratio (%) | Ductility Coefficient |
		Positive	Negative	Positive	Negative			
TS-1		269.6	262.4	283.0	279.4	2.39	6.75	2.82
TS-2		253.0	260.5	270.9	278.6	2.66	6.67	2.50
TS-3	Left	254.9	271.4	271.6	290.7	2.52	7.22	2.87
	Right	261.2	269.6	285.5	295.8	2.42	7.44	3.07
TS-4	Left	255.6	270.1	279.3	294.7	2.22	7.18	3.23
	Right	262.1	268.9	280.1	287.1	2.28	6.68	2.93

4.3. Energy Dissipation

Energy dissipation performance is usually evaluated by hysteretic energy dissipation and equivalent viscous damping coefficient, as given in Equations (2) and (3).

$$E = \frac{S_{(ABC+CDA)}}{S_{(OBE+ODF)}} \tag{2}$$

$$\zeta_{eq} = \frac{E}{2\pi} \tag{3}$$

where $S_{(ABC+CDA)}$ and $S_{(OBE+ODF)}$ are the area enclosed by the hysteretic loop and the summation of the triangle areas OBE and ODF, respectively. An idealized hysteresis loop is shown in Figure 17.
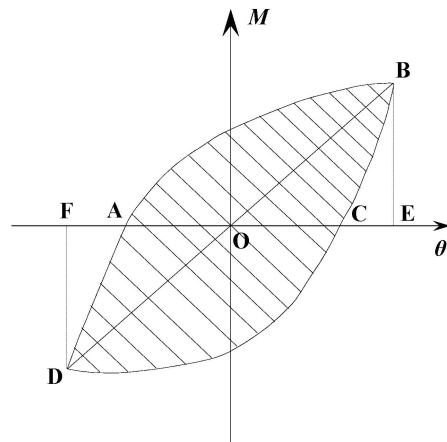

Figure 17. Idealized hy.teretic loop.

A comparison is made between specimens TS-1 and TS-2 in Figure 18a,b. Before the yield drift ratio, hysteretic energy dissipation of both specimens is almost none. The difference between the two specimens is almost ignorable. After the yield ratio, the equivalent viscous damping coefficient of TS-1 is higher than that of specimen TS-2 by 10–15%. This can also be due to the weakened stiffness of TS-2. Figure 18c,d compare the four curves of both sides of TS-3 and TS-4. The result shows a good coincidence of these curves, indicating that the factor of the connecting plate thickness can be ignored.

(**a**) Energy dissipation curve of TS-1 and TS-2

(**b**) Equivalent viscous damping curve of TS-1 and TS-2

(**c**) Energy dissipation curve of TS-3 and TS-4

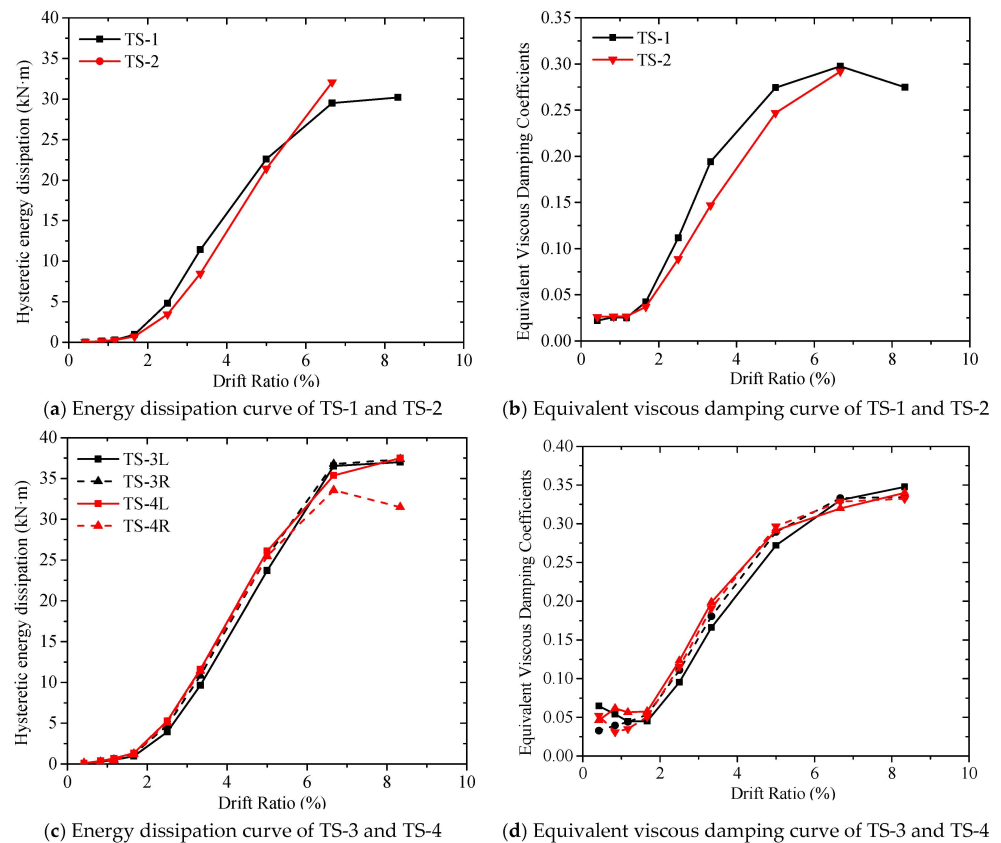(**d**) Equivalent viscous damping curve of TS-3 and TS-4

Figure 18. Energy dissipation of the specimens.

5. Numerical Analysis

For further investigation of the self-lock joints, finite element (FE) models were developed and numerical analysis was conducted based on commercial software ABAQUS (Ver.6.13).

5.1. Geometry, Material Properties, and Boundary Condition

The geometry of the FE models was based on the specimens above, as shown in Figure 19. These models consist of most parts of the specimens, including beams, columns, joint boxes, and connectors. Details of the connectors were also considered, including ring-teeth and cone surfaces. An opening was set on the joint box to simulate the weakening effect of the self-lock device. All components of the FE models were modeled with solid element C3D8R. In order to balance the computational efficiency and convergence, different mesh sizes are set for different parts of the joints: 40.0 mm for the module column, 20.0 mm for the floor and ceiling beam, 20.0 mm for the side of the node box, and 10.0 mm for the bottom plate where the self-locking connector is inserted. The mesh size for inserting the self-locking connector is the smallest, the mesh size of the sleeve is 8.0 mm, the mesh size of the insert rod and the taper card is 5.0 mm, and the mesh size of the ring tooth part is encrypted to 2.0 mm.
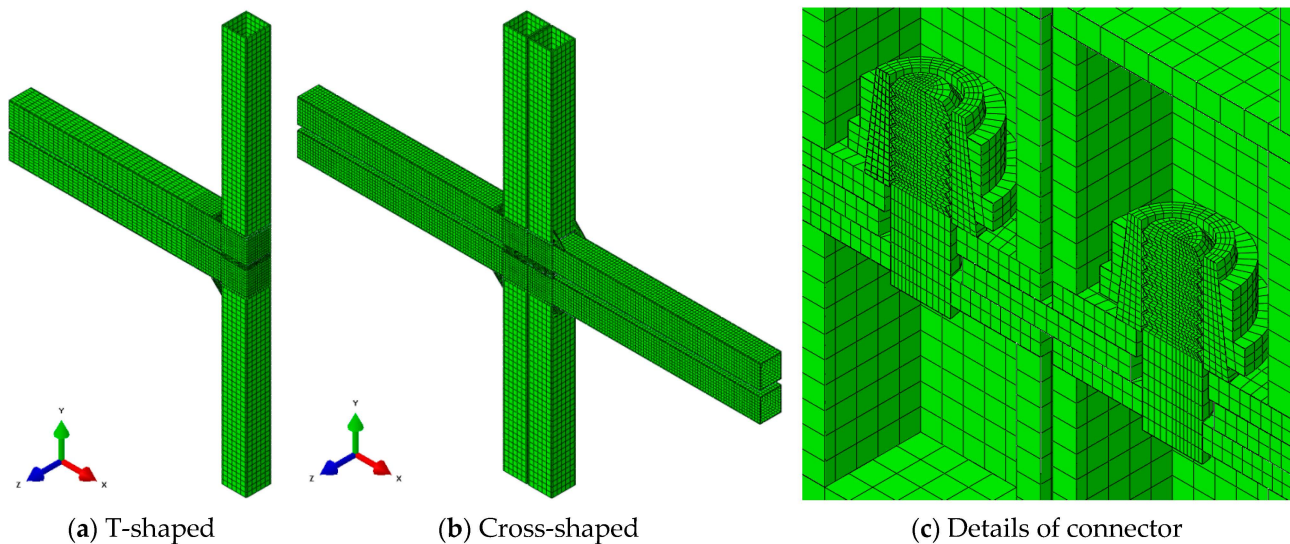

(**a**) T-shaped   (**b**) Cross-shaped   (**c**) Details of connector

Figure 19. FE models of self-lock joint.

The constraints of these parts were simulated based on the real condition. In an upper or lower module, beam, column, and stiffeners were tie-connected to the joint box to simulate the welding. But the interface between the upper and lower joint boxes was not tied. Instead, a surface contact pair was set to simulate the separation and slide of the interface. The normal behavior of the contact pair was set as the hard contact while the tangential behavior was set as the frictional contact. Based on previous research, the friction coefficient was set as 0.15 in this paper. Similar contact pairs were also set on the ring-teeth and cone surfaces of the connector.

The boundary condition of the FE models was also based on the experimental study. As shown in Figure 19, displacement constraints were applied at the top and bottom of the FE models. At the bottom of the lower column, Ux, Uy, and Uz displacement constraints were applied. At the top of the upper column, Ux and Uz displacement constraints were applied while Uy was released. A constant axial force was applied on the top of the models. The cyclic load was applied at the beam ends according to ATC-24. The rotations of the beam and column ends were not restricted. Uy displacement constraints were applied to the beam ends to prevent the out-of-plane rotation of the models.

The material properties were set based on the coupon test results above, as shown in Table 4 and Figure 20. Elastoplastic properties were applied to the FE meshes. To simulate the behavior under cyclic load, kinematic hardening was set for material properties.

Table 4. Material Properties of FE Models.

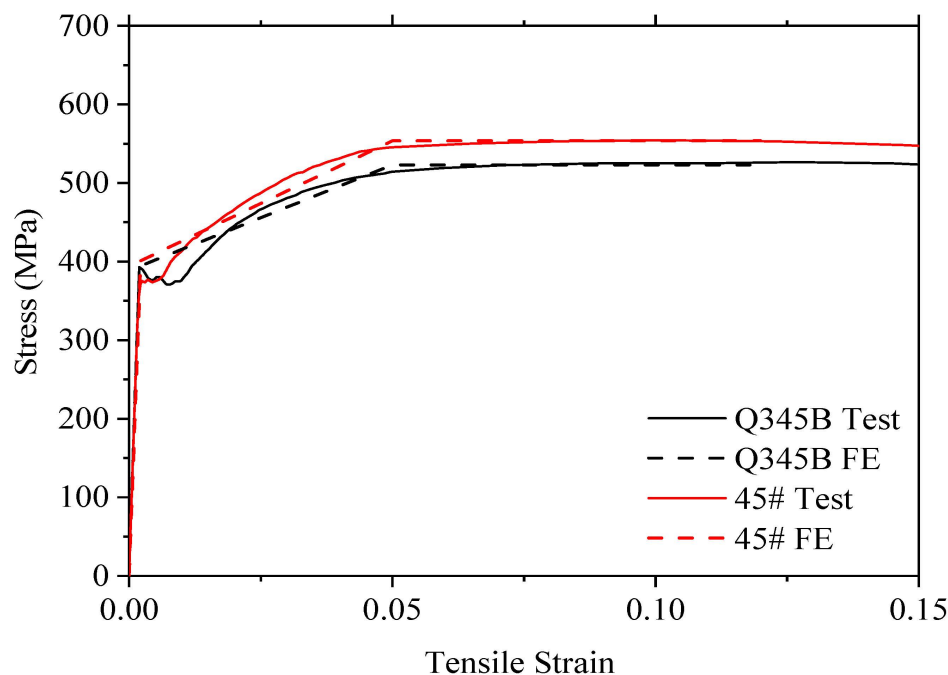| Parts	Elastic Modulus (N/mm^2)	Yield Strength (N/mm^2)	Ultimate Strength (N/mm^2)
Connector components	200.0	441.3	553.7
Steel plate	200.0	393.8	523.5

Figure 20. Elastoplastic material properties for FE models.

5.2. Validation

The FE models were analyzed with an implicit solver and the analysis results were validated with the test results. Figure 21 shows the validation of moment–drift ratio curves. In general, the FE curves fit well with the test ones. The hysteresis loops of FE and test curves are close except for the loops near the ultimate point. At the elastic and yield phases, the hysteresis loops of FE and test curves are in good agreement. During the strengthening phase, the loops of FE results are thinner than the test ones. This is due to the simplified model of elastoplastic material properties. As fractures are not considered in the FE material properties, the cracks on the beam sections cannot be simulated correctly. This results in the difference between the last loops.

Table 5 shows the strength and initial stiffness of FE and test results. The yield strength, maximum strength, and initial stiffness of the FE results fit well with the test ones. The maximum error of these important features was about 5.3%, which is acceptable to the authors.

Figure 22 shows the key observations on FE models and test results. The buckling and deformation at the root of the beams are simulated correctly. The high-stress areas in FE models, as shown as the grey-colored areas in Figure 22a,c, are the exact fractured areas in the test specimens. These indicate that the FE models are effective and can simulate the behavior of the novel self-lock joints correctly.
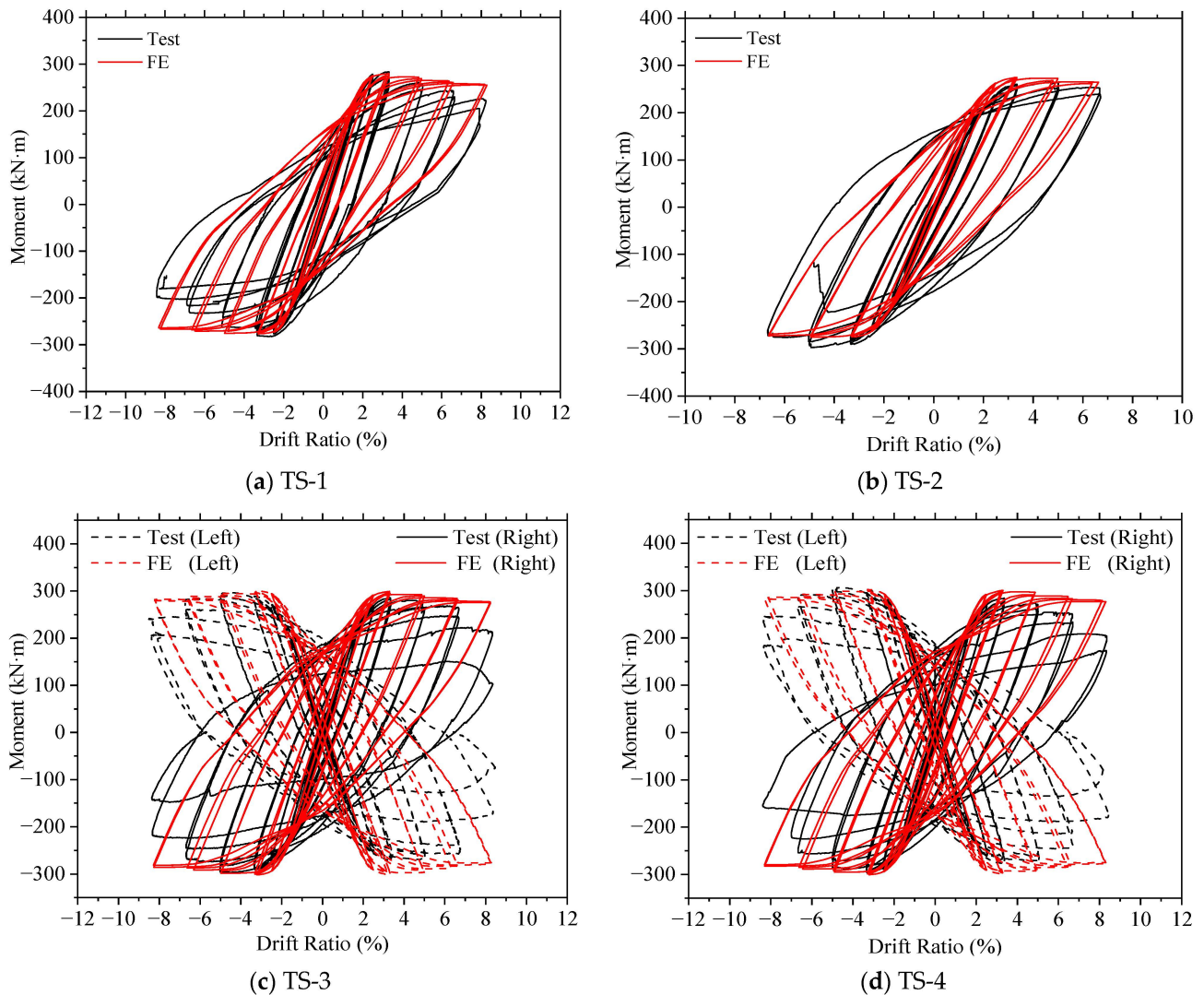
(**a**) TS-1

(**b**) TS-2

(**c**) TS-3

(**d**) TS-4

Figure 21. Validation of FE results.

Table 5. Comparison of Strength and Stiffness in FE and Test Results.

No	Yield Strength			Maximum Strength			Initial Stiffness		
	FE Result (kN·m)	Test Result (kN·m)	Error (%)	FE Result (kN·m)	Test Result (kN·m)	Error (%)	FE Result (kN·m/rad)	Test Result (kN·m/rad)	Error (%)
TS-1	271.2	266.0	2.0	279.4	281.2	0.6	13,395	13,543	−1.1
TS-2	262.7	256.8	2.3	274.6	274.8	<0.1	12,262	11,855	+3.4
TS-3	273.8	264.2	3.4	297.9	285.9	4.2	13,868	13,596	+2.0
TS-4	270.7	265.1	2.1	301.4	287.6	5.0	13,997	14,780	−5.3

5.3. Parameter Analysis

For further investigation of the seismic behavior of this type of joint, twenty FE models were developed to evaluate the factors that may affect the performance. Several inner-module and inter-module factors are considered, including the thickness of the side and end plate of joint boxes, the diameter of the stud, the unlocking device, and the inner plate, as shown in Figure 23. Table 6 shows the details of the FE models. Considering the "Strong joint" principle, the thickness of the joint region should not be lower than the thickness of columns and beams. In this case, the minimum thickness of the joint region is set as 10 mm.
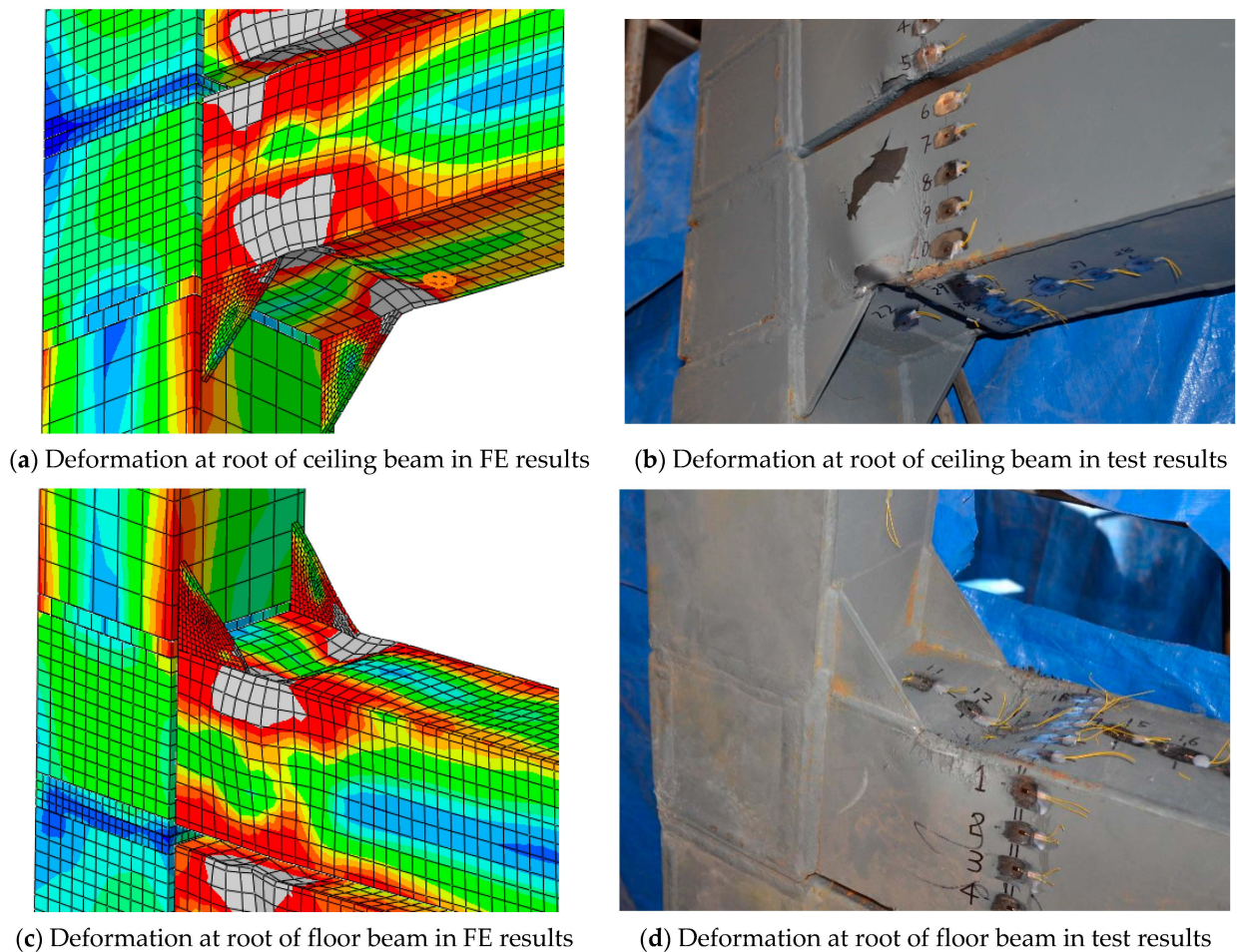
(**a**) Deformation at root of ceiling beam in FE results   (**b**) Deformation at root of ceiling beam in test results

(**c**) Deformation at root of floor beam in FE results   (**d**) Deformation at root of floor beam in test results

Figure 22. Observations on FE models and test specimens.
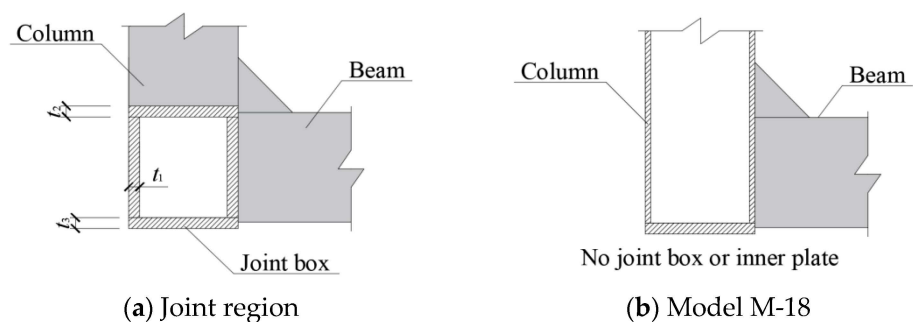

(**a**) Joint region   (**b**) Model M-18

Figure 23. Joint region of the FE models.

The results show that all models exhibit similar yield and maximum strength except for model M-18. The thickness of the joint boxes and the diameter of the stud do not affect the strength of the joint significantly. As shown in Figure 24, yield the strength remains at about 260–270 kN·m while the thickness of the joint box changes. The reason is that the failure mode of the joint is buckling at the root of the beam. The strength joint is determined by the beam sections instead of joint boxes. The model M-18 is a joint model without joint boxes. The beams are directly welded to the square hollow section columns. The yield and maximum strength of M-18 is lower than that of other models by about 10%. Figure 25 compares the deformation on models M-6 and M-18. The side thickness of the joint boxes in model M-6 is 10.0 mm, which is the same as the thickness of the column in model M-18. The failure mode of this model is due to the failure of the column. Plastic out-of-plane deformation occurs at the root of the column. Also, the initial stiffness of the model is lower.

This indicates that the joint boxes are essential for this type of joint. Joints that welded the beams directly to the columns are not recommended.

Table 6. Details of FE Models.

No	t_1 (mm)	t_2 (mm)	t_3 (mm)	D (mm)	Unlocking Device	Yield Strength (kN·m)	Maximum Strength (kN·m)	Initial Stiffness (kN·m/rad)
M-1	20	16	16	50	-	269.8	285.0	13,834
M-2	18	16	16	50		269.5	284.5	13,724
M-3	16	16	16	50	-	269.1	284.2	13,628
M-4	14	16	16	50		266.4	281.9	13,430
M-5	12	16	16	50	-	264.9	280.0	13,265
M-6	10	16	16	50	-	262.9	278.1	13,063
M-7	16	16	16	50	Yes	263.8	282.0	12,288
M-8	16	20	16	50	-	269.6	283.8	13,726
M-9	16	18	16	50		269.4	284.5	13,695
M-10	16	14	16	50		268.8	284.1	13,560
M-11	16	12	16	50	-	267.8	283.7	13,531
M-12	16	10	16	50	-	267.2	282.8	13,516
M-13	16	16	20	50	-	269.4	284.1	13,683
M-14	16	16	18	50		269.1	284.3	13,665
M-15	16	16	14	50		269.0	284.2	13,556
M-16	16	16	12	50	-	265.5	281.1	13,452
M-17	16	16	10	50	-	265.8	282.4	13,383
M-18		No joint box			-	235.1	255.6	12,360
M-19	20	20	20	60	-	268.2	284.3	13,656
M-20	20	20	20	40	-	267.7	283.9	13,523

(**a**) t_1

(**b**) t_2

(**c**) t_3

Figure 24. Effects of thickness.

(**a**) Model M-6 (with joint boxes)

(**b**) Model M-18 (without joint boxes)
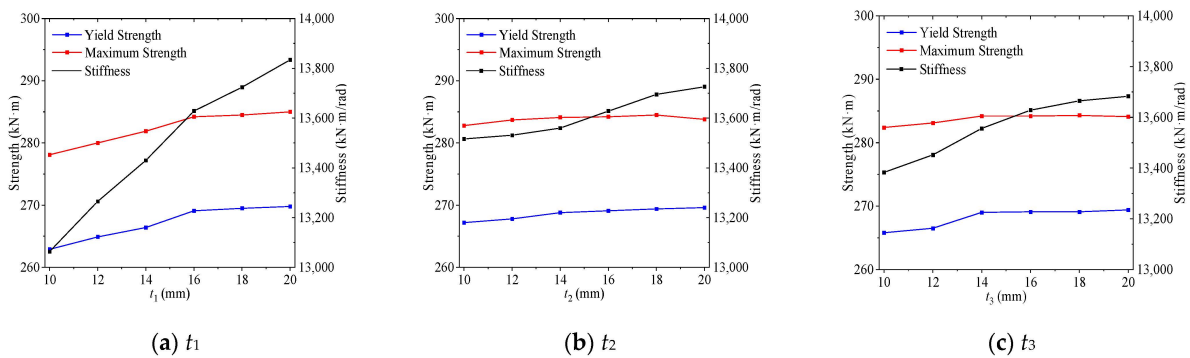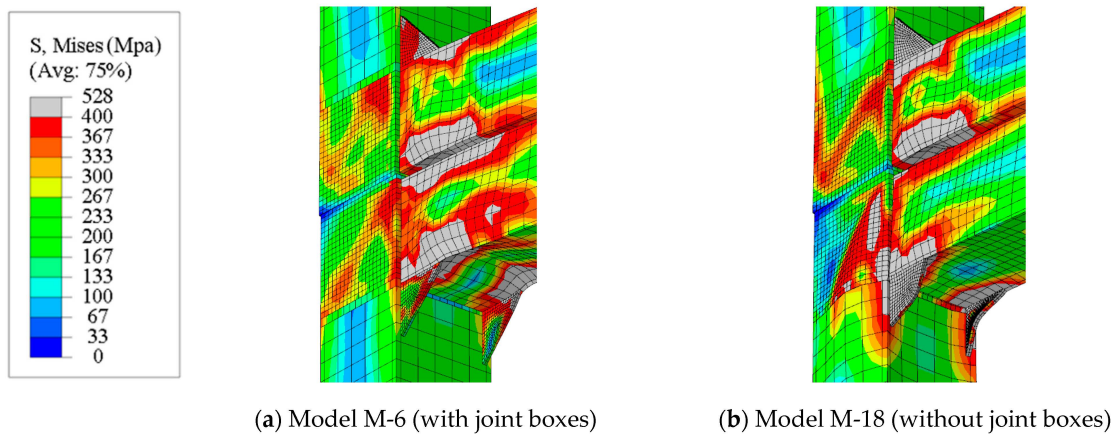
Figure 25. Comparison of deformation on model M-6 and M-18.

6. Conclusions

A type of self-lock joint for modular steel construction was tested and analyzed in this paper. An experimental study, including functional and cyclic loading tests, was conducted on four full-scale specimens. The finite element (FE) models were developed and validated through the test results. The following conclusions are made based on the test and analysis results.

(a) The demountable function of the self-lock joints was validated through the test program. The results show that the mechanism of the joints works well. The connecting and demounting function of the novel joints can be realized in modular steel construction.

(b) The seismic behavior of the self-lock joints was investigated through experimental study. The results show that these types of novel joints exhibit exceptional seismic behavior, and they can be defined as semi-rigid full-strength joints. The strength of the joint is determined by the beam sections. Due to the maintenance opening on the joint boxes, the unlocking device decreases the stiffness of the joint by 10%, but this does not affect the yield and maximum strength. The thickness of the connecting plate does not affect the seismic behavior of cross-shaped joints.

(c) Numerical analysis was conducted based on the tests. FE models were developed and validated through the test. Comparisons of the load–drift ratio curve, strength, stiffness, and deformation were made between the FE and test results. The comparisons show that the FE result fits well with the test ones. The main conclusions of the parameter analysis show that the absence of the joint box reduces the initial stiffness of the joint, and the thickness of the joint box plate and the diameter of the stud do not significantly affect the strength of the joint. Therefore, for the design of a demountable self-locking joint, it is necessary to set joint boxes. The plate size of the joint box can be considered according to the conventional plate size, that is, not less than the thickness of the beam and column.

Author Contributions: Conceptualization, L.Z. and Y.D.; Methodology, X.-M.D. and L.Z.; Validation, X.-M.D.; Formal analysis, X.-M.D. and F.-W.S.; Investigation, L.Z.; Writing—original draft, X.-M.D. and F.-W.S.; Writing—review & editing, H.-W.Z.; Visualization, H.-W.Z.; Funding acquisition, L.Z. and Y.D. All authors have read and agreed to the published version of the manuscript.

Data Availability Statement: Data are contained within the article.

Conflicts of Interest: Author Xiao-Meng Dai was employed by the company China Railway Construction Bridge Engineering Bureau Group Corporation, Ltd. The remaining authors declare that the research was conducted in the absence of any commercial or financial relationships that could be construed as a potential conflict of interest.

References

1. Deng, E.F.; Zong, L.; Ding, Y.; Dai, X.M.; Lon, N.; Chen, Y. Monotonic and cyclic response of bolted connections with welded cover plate for modular steel construction. *Eng. Struct.* **2018**, *167*, 407–419. [CrossRef]
2. Lawson, R.M.; Ogden, R.; Goodier, C. *Design in Modular Construction*; CRC Press: Boca Raton, FL, USA, 2014.
3. Chen, Z.H.; Liu, J.D.; Yu, Y.J. Experimental study on interior connections in modular steel buildings. *Eng. Struct.* **2017**, *147*, 625–638. [CrossRef]
4. Chen, Z.; Liu, J.; Yu, Y.; Zhou, C.; Yan, R. Experimental study of an innovative modular steel building connection. *J. Constr. Steel Res.* **2017**, *139*, 69–82. [CrossRef]
5. Lacey, A.W.; Chen, W.; Hao, H.; Bi, K. Structural response of modular buildings—An overview. *J. Build. Eng.* **2018**, *16*, 45–56. [CrossRef]
6. Liu, X.C.; Pu, S.H.; Zhang, A.L.; Xu, A.X.; Ni, Z.; Sun, Y.; Ma, L. Static and seismic experiment for bolted-welded joint in modularized prefabricated steel structure. *J. Constr. Steel Res.* **2015**, *115*, 417–433. [CrossRef]
7. Sanches, R.; Mercan, O.; Roberts, B. Experimental investigations of vertical post-tensioned connection for modular steel structures. *Eng. Struct.* **2018**, *175*, 776–789. [CrossRef]

8. Fest, E.; Shea, K.; Domer, B.; Smith, I.F. Adjustable tensegrity structures. *J. Struct. Eng. ASCE* **2003**, *129*, 515–526. [CrossRef]
9. Du, X.L.; Wang, W.; Chan, T.M. Seismic design of beam-through steel frames with self-centering modular panels. *Eng. Struct.* **2018**, *141*, 179–188. [CrossRef]
10. Dai, X.M. Research on Seismic Behavior and Design Method of Self-Lock Plug-In Joints in Modular Steel Construction. Ph.D. Thesis, Tianjin University, Tianjin, China, 2021.
11. Chen, Z.; Niu, X.; Liu, J.; Khan, K.; Liu, Y. Seismic study on an innovative fully bolted beam-column joint in prefabricated modular steel buildings. *Eng. Struct.* **2021**, *234*, 111875. [CrossRef]
12. Du, H.; Zhao, P.; Wang, Y.; Sun, W. Seismic experimental assessment of beam through beam-column connections for modular prefabricated steel moment frames. *J. Constr. Steel Res.* **2022**, *192*, 107208. [CrossRef]
13. Dai, X.M.; Zong, L.; Ding, Y.; Li, Z.X. Experimental study on seismic behavior of a novel plug-in self-lock joint for modular steel construction. *Eng. Struct.* **2019**, *181*, 143–164. [CrossRef]
14. *GB/T 228.1-2010*; Metallic Materials-Tensile Testing-Part 1: Method of Test at Room Temperature. SAC (Standardization Administration of the People's Republic of China): Beijing, China, 2010. (In Chinese)
15. *GB/T 699-2015*; Quality Carbon Structure Steels. SAC (Standardization Administration of the People's Republic of China): Beijing, China, 2015. (In Chinese)
16. *GB/T 1591-2018*; High Strength Low Alloy Structural Steels. SAC (Standardization Administration of the People's Republic of China): Beijing, China, 2018. (In Chinese)
17. Srisangeerthanan, S.; Hashemi, M.J.; Rajeev, P.; Gad, E.; Fernando, S. Numerical study on the effects of diaphragm stiffness and strength on the seismic response of multi-story modular buildings. *Eng. Struct.* **2018**, *163*, 25–37. [CrossRef]
18. *ATC-24*; Guidelines for Cyclic Seismic Testing of Components of Steel Structures. ATC (Applied Technology Council): Redwood City, CA, USA, 1992.
19. *BS EN 1993-1-8:2005*; Design of Steel Structures—Part 1–8: Design of Joints. CEN (European Committee for Standardization): London, UK, 2005.